Dynamics of deformation and pinch-off of a migrating compound droplet in a tube

Manash Pratim Borthakur,[1] Gautam Biswas,[1,*] and Dipankar Bandyopadhyay[2]

[1]*Department of Mechanical Engineering, Indian Institute of Technology Guwahati, Guwahati 781039, India*
[2]*Department of Chemical Engineering, Indian Institute of Technology Guwahati, Guwahati 781039, India*

A computational fluid dynamic investigation has been carried out to study the dynamics of a moving compound droplet inside a tube. The motions associated with such a droplet is uncovered by solving the axisymmetric Navier-Stokes equations in which the spatiotemporal evolution of a pair of twin-deformable interfaces has been tracked employing the volume-of-fluid approach. The deformations at the interfaces and their subsequent dynamics are found to be stimulated by the subtle interplay between the capillary and viscous forces. The simulations uncover that when a compound drop composed of concentric inner and outer interfaces migrates inside a tube, initially in the unsteady domain of evolution, the inner drop shifts away from the concentric position to reach a morphology of constant eccentricity at the steady state. The coupled motions of the droplets in the unsteady regime causes a continuous deformation of the inner and outer interfaces to obtain a configuration with a (an) prolate (oblate) shaped outer (inner) interface. The magnitudes of capillary number and viscosity ratio are found to have significant influence on the temporal evolution of the interfacial deformations as well as the eccentricity of the droplets. Further, the simulations uncover that, following the asymmetric deformation of the interfaces, the migrating compound droplet can undergo an uncommon breakup stimulated by a rather irregular pinch-off of the outer shell. The breakup is found to initiate with the thinning of the outer shell followed by the pinch-off. Interestingly, the kinetics of the thinning of outer shell is found to follow two distinct power-law regimes—a swiftly thinning stage at the onset followed by a rate limiting stage before pinch-off, which eventually leads to the uncommon breakup of the migrating compound droplets.

I. INTRODUCTION

The controlled production of monodisperse droplets using microchannels or capillary tubes has become an important process of late owing to their frequent appearance in cutting-edge applications such as the aerosol detection [1], spray atomizers [2], single cell analysis [3,4], PCR studies [5,6], microreactors [7,8], and emulsifiers [9], among others. In particular, the production of stable compound droplets or double emulsions has become one of the major areas of research, owing to their capacity in the continual release of active ingredients in the various products and processes such as the cosmetics, food, agriculture, and pharmaceuticals [10,11]. The compound droplets are, in general, composed of a primary large droplet impregnated with a single or a collection of smaller droplets. The configuration ensures that the smaller liquid droplets can be loaded with a specialty chemical inside the encapsulating larger droplet and kept isolated from the surroundings with the help of the wrapping of the outer immiscible fluid [12]. The size of the compound droplets vary typically in the range from a few micrometers to a few millimeters [13]. In general, a large collection of such droplets are synthesized inside fluidic medium through various emulsification processes [14–18]. Recent studies suggest that these droplets can be employed for next-generation targeted drug delivery [10,19], advanced materials processing [20,21],

phase separation [22,23], handling of hazardous materials [24], among others.

The prior art indicates that while in some of the applications the breakup of the compound droplet decides their performance, in other applications the stability of them ensure the viability. It is thus of paramount importance to understand the spatiotemporal hydrodynamic behavior of the compound droplets moving inside a tube to track and control the deformation and subsequent breakup of them. Importantly, the formation and breakup of compound droplets can be very different from the same of the single droplets flowing inside a cylindrical tube. For example, a number of previous theoretical [25–27], numerical [28–34], and experimental [35–37] investigations show the various deformation and break up features of the single droplet flows inside a tube. These behaviors are found to be very different from the response of the compound droplets under a variety of flow conditions [14–18]. In particular, the uniqueness of the interfacial deformations and subsequent pinch-off mechanisms during the extensional and shear flows [38–43], spreading [44–50], under the effects of surfactants [51,52] and constrictions [53,54], and also under confinement [53,54] have been explored so far in a greater detail. Importantly, while most of the afore stated studies have explored the concentric compound drops, a handful of studies have also focused on the dynamics of eccentric compound droplets [55–57].

However, there are hardly any studies that explore the transient evolution and the subsequent hydrodynamics of compound drops moving inside a capillary tube. In such a
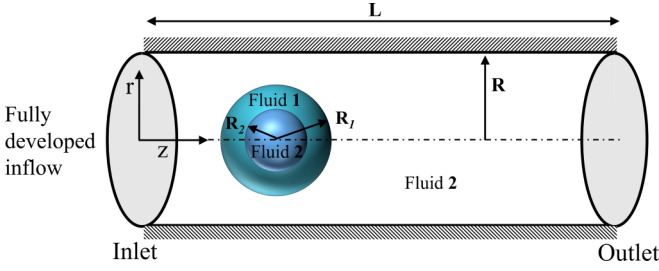
---

*gtm@iitg.ernet.in

FIG. 1. Schematic diagram showing the computational domain (not to scale) and boundary conditions in cylindrical coordinates system (r,z,θ).

scenario, the physics associated with the interplay between the surface tension forces at the deforming interfaces alongside the frictional influence of the fluids inside and of the deforming compound droplet can be an interesting subject for fundamental study. A recent work [58] has attempted to provide an analytical solution for the motion of a compound drop in a long circular tube in the Stokes flow limit at the low Reynolds number. However, the detailed spatiotemporal dynamics of the coupled twin-deformable interface of the compound drops translating inside a tube is yet to be explored in detail. In the present work, we make an attempt to uncover the spatiotemporal dynamics of a compound droplet migrating inside a tube. We employ the computational fluid dynamic framework to solve the axisymmetric Navier-Stokes equations and unveil the influence of the various thermodynamic and kinetic parameters on the deformation and breakup of such droplets. In particular, starting with a configuration shown in the Fig. 1 , we focus on the positions of the inner and outer droplets in the unsteady and steady regimes of the dynamics, which helps in predicting the kinetics of the deformation of the interfaces and the conditions for the pinching off of the outer shell of the droplet. Interestingly, the kinetics of the thinning of outer droplet is found follow distinct power-law regimes in which the onset is associated with a swiftly thinning stage followed by a rate limiting stage before pinch-off. The study shows that controlling of the later stage decides the formation of stable or unstable compound droplets wherein the inner drop is either protected or exposed to the surroundings. The results reported can be of significance for the microfluidic prototypes that targets using stable or unstable compound droplets useful for drug delivery, microreactor, cosmetic, and pharmaceutical applications.

The rest of the study is organized as follows. In Sec. II we outline the formulation of the problem, and in Sec. III we discuss the validation of the present numerical solver. The results are presented in Sec. IV, and concluding remarks have been drawn in Sec. V.

II. FORMULATION OF THE PROBLEM

A representative diagram of the computational domain adopted is presented in Fig. 1. We consider a two-component compound droplet placed inside a capillary tube of radius R and length L. The inner drop fluid and the ambient fluid are considered to be the same, thereby simplifying the dynamics to a two-phase interfacial flow system. This configuration

typically represents water-oil-water (W/O/W) or oil-water-oil (O/W/O) compound droplets [59,60]. Initially, the outer and inner interfaces are considered as concentric spheres of radius R_1 and R_2, respectively. The fluids are considered Newtonian, incompressible, and mutually immiscible. A fully developed inflow of the ambient fluid is imposed at the inlet of the capillary tube. A cylindrical coordinate system (r,z,θ) is adopted considering the dynamics to be axisymmetric so that the problem is independent of θ, where (r,z,θ) are the radial coordinate, axial coordinate, and azimuthal angle, respectively. The length of the computational domain is taken as $30R$ in the axial direction so as to ensure that the results are not influenced by outflow boundary conditions.

A. Governing equations

The governing equations of the problem correspond to the conservation of mass and momentum, respectively, as

$$\nabla \cdot \vec{\mathbf{V}} = 0, \tag{1}$$

$$\rho[\partial\vec{\mathbf{V}}/\partial t + (\vec{\mathbf{V}} \cdot \nabla)\vec{\mathbf{V}}] = -\nabla P + \sigma\kappa\mathbf{n}\delta + \nabla \cdot [\mu(\nabla\vec{\mathbf{V}} + \nabla\vec{\mathbf{V}}^T)], \tag{2}$$

and the following advection equation for volume fraction, α of fluid A:

$$\partial\alpha/\partial t + \nabla \cdot (\vec{\mathbf{V}}\alpha) = 0. \tag{3}$$

In the above equations, $\vec{\mathbf{V}} = (u,v)$ represents the velocity field with components u,v along z and r axis, respectively. The pressure field is denoted by p and α represents the volume fraction of fluid A, σ represents the interfacial tension, which is assumed to be spatially uniform and constant with time, δ is the Dirac δ function, and $\kappa = \nabla \cdot \mathbf{n}$ is the interfacial curvature, in which $\mathbf{n}$ is the outward pointing unit normal to the interface.

The density and viscosity are computed on the basis of volume fraction of the fluids as

$$\rho = \alpha\rho_1 + (1 - \alpha)\rho_2, \tag{4}$$

$$\mu = \alpha\mu_1 + (1 - \alpha)\mu_2, \tag{5}$$

where ρ_1 and μ_1 are the density and viscosity of the shell fluid, whereas ρ_2 and μ_2 are the corresponding density and viscosity of the ambient (and core) fluid.

B. Numerical procedure

We solve the axisymmetric incompressible Navier-Stokes equations using an open source code Basilisk [61]. Basilisk is a successor to the popular open source solver Gerris [62] and has been extensively benchmarked on a wide range of problems involving interfaces [63–65]. It features an incompressible Navier-Stokes solver that is second-order accurate in both time and space. The discretization of the governing equations are handled using the finite volume technique. The Bell-Colella-Glaz [66] scheme is employed for treating the advection terms and the pressure-correction method is used for velocity-pressure coupling. The interface between these two phases is tracked with a volume-of-fluid method [67]. A consistent and precise description of the surface forces
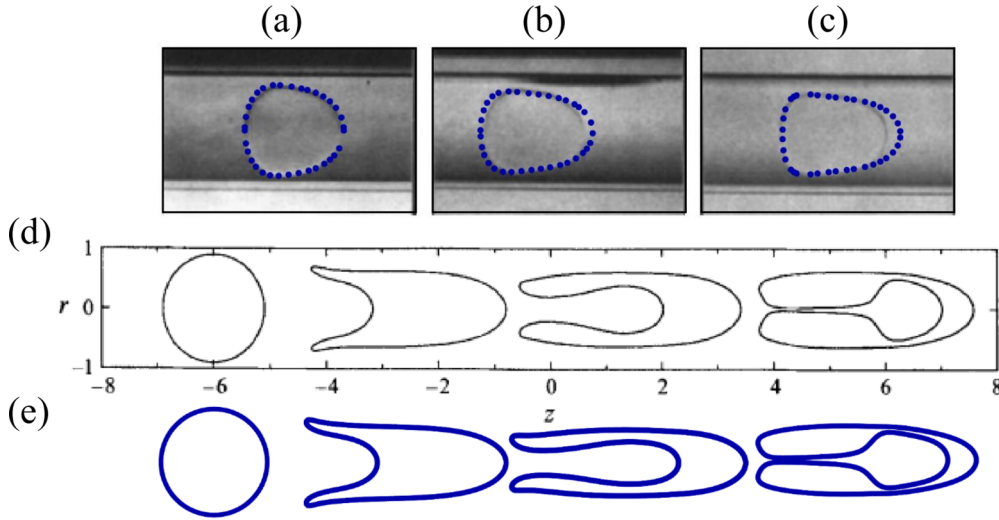
FIG. 2. Comparison of experimental results of Olbritch and Kung [71] with present computations (blue line) for steady shapes of a droplet migrating inside a capillary tube at (a) Ca = 0.05, (b) Ca = 0.10, and (c) Ca = 0.16. The operating parameters are $\eta = 1.01$ and $a = 0.95$. (d) Temporal evolution of droplet shapes obtained by Tsai and Miksis [29]. (e) The shapes obtained from the present computations using the same configuration of Tsai and Miksis [29]. The corresponding time instants are $t^* = 0, 2, 4$, and 6.

is implemented with the continuum surface force model for surface tension [68]. Extensive details on the implemented methods and convergence studies are available in Ref. [63].

C. Initial and boundary conditions

To solve the governing equations, the following initial and boundary conditions are implemented. The simulations are initialized by placing a concentric compound droplet in a parabolic flow inside the tube. The drop is placed at a distance of $2.5R$ from the inlet location. Although the initialization of the concentric drop is somewhat artificial, we expect the steady-state deformation and droplet eccentricity to remain invariant to the initial conditions. This approach of initializing a circular droplet in a flowing fluid inside a tube has been adopted earlier, by many researchers [32,34,69]. A fully developed velocity is imposed at the inlet of the capillary tube ($z = 0$) given by $u(r) = 2V_{avg}(1 - \frac{r^2}{R^2})$ and $v(r) = 0$, where V_{avg} is the average velocity of the imposed inflow. The walls of the capillary tube are modeled as rigid surfaces with no-slip and no-penetration conditions, i.e. $u = v = 0$ at $r = R$. At the tube outlet, Neumann conditions for velocity and a fixed pressure is applied for the outflow condition as $\partial u/\partial z = \partial v/\partial z = 0$ and $p = p_0$ at $z = L$. The computations are stopped when the drop is at a distance of $2R$ from the outlet. This ensures that the flow disturbances produced by the drop do not reach both the inlet and the outlet.

D. Scaling

The radius of the tube, R, and average velocity of imposed flow at inlet V_{avg} are taken as the characteristic length and velocity scales. The corresponding timescale comes out as R/V_{avg}. The properties of shell fluid, ρ_1 and μ_1, are employed as the density and viscosity scales, respectively. The results obtained from our computations are presented in terms of nondimensional parameters. The relevant dimensionless

numbers pertinent to our problem are the capillary number Ca $= \mu_1 V_{avg}/\sigma$, Reynolds number Re $= \rho_1 V_{avg} R/\mu_1$, density ratio $\gamma = \rho_2/\rho_1$, viscosity ratio $\eta = \mu_2/\mu_1$, drop aspect ratio $a = R_1/R$, and the shell thickness ratio $k = R_2/R_1$. The capillary number represents the ratio of viscous force over surface tension force. In our study, the Reynolds number, which represents the relative magnitude of inertia over viscous forces, is maintained at unity (Re $= 1$) for the entire range of our computations. Furthermore, as we concentrate on the dynamics of neutrally buoyant drops ($\gamma = 1$), the influence of gravity can be safely neglected.

E. Fluid properties

The inner drop fluid and the outer ambient fluid are considered to be same thereby the problem is simplified as the study of a two-fluid system. The shell fluid is chosen to be an aqueous solution of glycerine. The ambient fluid (and inner core fluid) is considered as different grades of silicone oil [70]. The density contrast for the chosen fluid combinations is negligible and hence in our entire study, we consider the density ratio γ to be unity.

III. VALIDATION OF NUMERICAL PROCEDURE

A. Comparison with literature

The numerical solver adopted for the present study is thoroughly validated by comparing our results with earlier investigations. Figures 2(a), 2(b) and 2(c) presents the steady shapes of a droplet migrating inside a capillary tube as observed by Olbritch and Kung [71] for three different Ca. The corresponding shapes from the present computations are superimposed on top of the experimental images. It can be seen that the drop profile shows good agreement for Ca = 0.05 and 0.10. However, a slight deviation is seen for Ca = 0.16. Additionally, we reproduce the shapes obtained by Tsai and Miksis [29] for droplets approaching breakup inside capillary
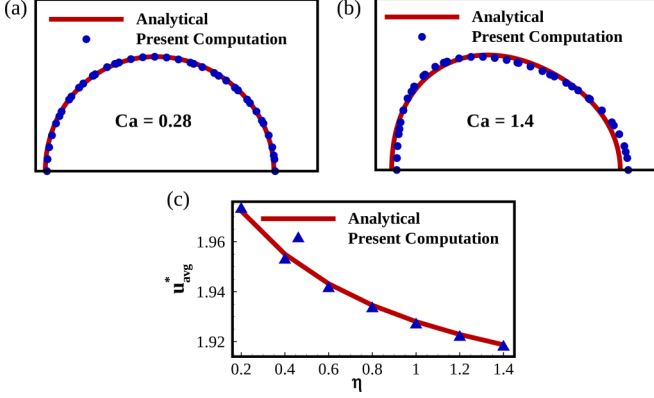
FIG. 3. Quantitative comparison of drop shapes and average droplet velocity between theoretical solutions of Nadim and Stone [Eq. (6)] and present computations. Panels (a) and (b) show the drop shapes for Ca = 0.28 and 1.4, respectively, while other parameters are fixed at $\eta = 1$ and $a = 0.3$. Panel (c) demonstrates the variation of $u^*_{\rm avg}$ with η keeping Ca and a fixed at 0.2 and 0.3, respectively.

tubes [Fig. 2(d)]. The results from our simulations, as shown in Fig. 2(e), demonstrate good qualitative agreement with the reported shapes of Tsai and Miksis [29] for the time instants $t^* = 0, 2, 4$, and 6.

To gain more confidence on the numerical solver, we compare the drop shapes and average drop velocity obtained from the analytical solutions of Nadim and Stone [72] with the results from our present computations. The theoretical solutions of drop shapes and average velocity are given as [72]

$$s = 1 + {\rm Ca}\left(\frac{R_1}{R}\right)^2 \frac{10 + 11\lambda}{8(1+\lambda)}\left(\cos^3\theta - \frac{3}{5}\cos\theta\right),$$

$$u^*_{\rm avg} = 2.0\left[1 - \frac{2\lambda}{2+3\lambda}\left(\frac{R_1}{R}\right)^2\right], \tag{6}$$

where s and θ describe the drop interface relative to its center and $u^*_{\rm avg}$ denotes the average drop translation velocity. The results from our computations presented in Fig. 3 demonstrate good agreement with the theoretical predictions of Nadim and Stone [72].

B. Grid convergence studies

To ensure that the results are independent of grid resolution, we chose four grid meshes (8×240, 16×480, 32×960, and 64×1920). The test was conducted for a compound drop migrating under conditions of Ca = 0.5, $\eta = 0.2$, $a = 0.6$, and $k = 0.5$ and the average dimensionless velocity of the drop $u^*_{\rm avg}$ was compared as a function of dimensionless time t^* for the chosen grids as shown in Fig. 4. The steady velocities of the drop obtained are 1.526, 1.569, 1.584, and 1.588 for the four chosen grids, respectively. The difference of $u^*_{\rm avg}$ between grids 8×240 and 16×480 is around 2.8%, whereas the difference between the grid-meshes 32×960 and 64×1920 is less than 0.3%. Based on this, the grid-mesh of 32×960 has been adopted for this study to optimize the computational time without compromising the accuracy of the obtained results. The smallest dimensionless cell size for the chosen grid is 0.031. However, in Sec. IV D, the breakup of
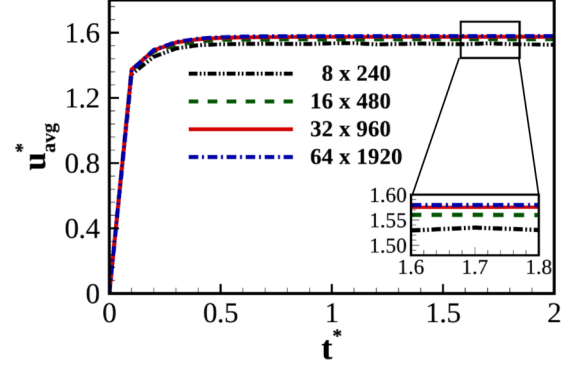

FIG. 4. Comparison of the average drop velocity for different grid sizes (8×240, 16×480, 32×960, and 64×1920) as a function of dimensionless time t^*. The operating parameters are Ca = 0.5, $\eta = 0.2$, $a = 0.6$, and $k = 0.5$.

compound droplets is explored, which is more sensitive to the grid resolution and requires further refinement. The numerical convergence of our results for drop breakup is demonstrated by performing additional grid resolution tests and are presented in Sec. IV D.

IV. RESULTS AND DISCUSSION

The following section presents a detailed study of the motion of the compound drops traversing inside a capillary tube and their associated dynamics. We initiate our study by considering the deformation dynamics of a compound droplet and exploring the hydrodynamics during its motion inside the capillary. Subsequently, we investigate the dynamics of breakup of the compound droplet. A large set of parameters are to be taken under consideration and in the results that follow, we have fixed the drop aspect ratio a at 0.6. The size of the inner drop has been taken to be half of the outer drop, i.e., $k = 0.5$.

The simulations are initialized by introducing a concentric drop in the capillary tube where a fully developed flow persists. The parabolic flow imposed at the tube inlet propels the drop to migrate across the tube (see Supplemental Material Video 1 [73]). The video suggests that during the flow, both the inner and outer interfaces deform in which the outer one elongates in the direction of the flow while the inner one does the same in the normal direction of the flow. Figure 5 presents the variables which are employed to quantitatively estimate the variation in the shapes of the interfaces during the motion. For example, the deformation index $D^* = (z_{\rm max} - z_{\rm min})/(r_{\rm max} - r_{\rm min})$ can be employed to evaluate the change of shape of a droplet along the flow direction (toward the z axis), where $D^* = 0$ as well as along the normal to the flow direction (toward the r axis), where $D^* < 0$. Additionally, the inner drop moves away from the initial concentric position, which can be quantified in terms of an eccentricity index $e^* = zi_{\rm cen} - zd_{\rm cen}$, where $zi_{\rm cen}$ is the area averaged center of the inner drop and $zd_{\rm cen}$ is the area averaged center of the entire drop. Owing to the drop eccentricity e^*, the outer shell thickness of a compound drop does not remain spatially uniform. In what follows, the temporal evolution of deformation index D^* and eccentricity index e^* have been explored for a wide range of parameters to
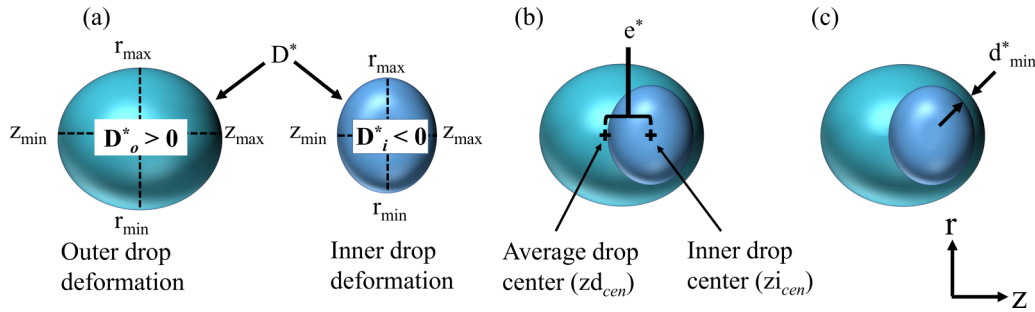
FIG. 5. The computed parameters used to describe the dynamics of compound droplets. (a) Deformation index (D_i and D_o) corresponding to inner and outer drop interfaces. (b) Drop eccentricity (e^*). (c) Minimum shell thickness d^*_{min}.

uncover the steady and unsteady deformation dynamics of the compound droplets, as shown in Secs. IV B and IV C. Further, the minimum distance between the inner and outer interfaces is defined as d^*_{min}, which helps in identifying the zone of pinching off of the outer shell. Thus, the temporal variation of d^*_{min} unveils the breaking and pinch-off kinetics of the compound droplets, as shown in Sec. IV D.

A. Temporal evolution of compound droplets

We consider the dynamics of a compound droplet and analyze its temporal evolution under conditions of Ca = 0.5 and $\eta = 0.2$. Figures 6(a) and 6(b) (and Supplemental Material Video 1 [73]) present snapshots of the compound droplet during its unsteady and steady states of evolution. The temporal evolution of the deformation parameter D^* and drop eccentricity e^* are shown in Figs. 6(c) and 6(d). The figures suggest that at the onset, the outer drop starts deforming with time in the direction of the flow, which generates a nonuniform curvature of the outer interface to compensate for the interfacial shear stresses. Figure 6(a) depicts the pressure field across the interfaces of a moving compound drop, which suggests that the pressure drop across the interfaces is inversely related to the curvature radius, as defined by the

Young-Laplace equation. The minimum curvature radius of the deformed outer droplet interface at the front and rear ends corresponds to the regions of maximum pressure drops. Further, the minimum pressure drop occurs approximately normal to the flow direction where the interfaces are rather flat and the curvature radius is maximum. Interestingly, the reduction in pressure in the normal direction of the flow stimulates the inner drop to deform perpendicular to the flow direction. It can be clearly observed from Fig. 6(c) that the deformation index D^* for the outer drop increases with time in the unsteady domain of evolution and attains a constant magnitude, thereby indicating a steady state with constant elongation axially. However, the magnitude of D^* is negative for the inner drop signifying an unsteady deformation along the perpendicular axis at the initial stages of evolution. As time progresses, the inner drop also reaches a steady state with constant deformation normal to the flow direction. Figure 6(b) presents the streamline patterns inside the compound droplet after it has attained steady state. The flow streamlines represent a set of circulation loops demonstrating the pattern of momentum transfer between the inner and outer interfaces of the compound droplet. Certainly, the temporal variation in the strength of the vorticities of these recirculations in the unsteady and steady domain of evolution decide the extent of mass, heat, and momentum transport across the interfaces. Additionally, it can be clearly perceived that the inner drop moves away from its concentric position and finally stabilizes near the "nose" of the outer drop. This can be attributed to the fact that the inner drop experiences lower drag due to its smaller size whereas the outer drop encounters higher drag force due to its larger size and proximity to the tube walls. This allows the smaller inner drop to migrate faster as compared to the larger outer drop thereby leading to an eccentric configuration with time. The evolution of the drop eccentricity e^* plotted in Fig. 6(d) demonstrates that the drop eccentricity initially rises sharply and saturates to a steady value with time. The faster moving inner drop is counteracted by the viscous drag of the thin shell fluid near the "nose," thereby reducing its velocity with time and hence the drop attains a fixed e^* after migrating for some period inside the capillary.
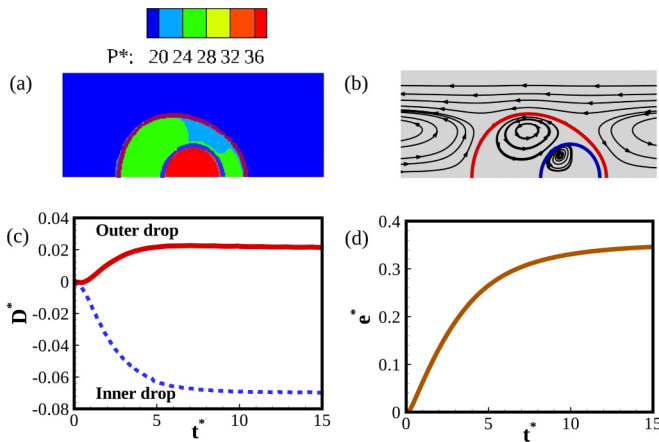

FIG. 6. Temporal evolution of the compound droplet under conditions of Ca = 0.5 and $\eta = 0.2$. Panel (a) represents the pressure field inside the compound droplet, panel (b) shows the streamline patterns inside the drop at steady state, panel (c) shows the variation of deformation index D^* with time for the inner and outer drop, and panel (d) presents the evolution of drop eccentricity with time.

B. Effect of capillary number

To understand the influence of capillary number on the dynamics of compound droplets, we perform simulations
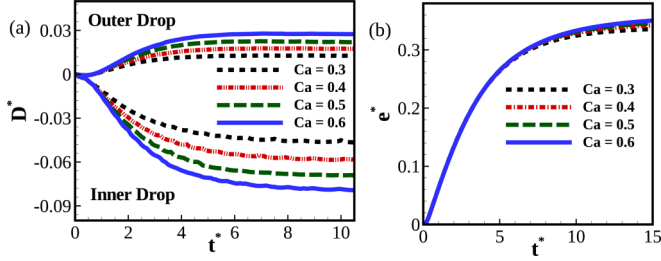
FIG. 7. Effect of capillary number on the (a) deformation of inner and outer drop and (b) eccentricity of the drop. The viscosity ratio η is kept fixed at 0.1.

FIG. 9. Effect of viscosity ratio on the (a) deformation of inner and outer drop and (b) eccentricity of the drop. The capillary number is kept fixed at 0.5.

by varying Ca from 0.3 to 0.6 while keeping η fixed at 0.2. The evolution of D^* and e^* with variation of capillary number is presented in Figs. 7(a) and 7(b), respectively. With increase in the capillary number, the dominance of capillary force over viscous resistance is reduced. In consequence, the deformations of both the inner and outer increase increase. Additionally, under these circumstances, the inner drop undergoes significantly higher deformation than the outer drop. This can be elucidated by considering the smaller curvature of the inner drop compared to the outer drop, which demands a larger interfacial strength to maintain the curvature of the inner drop. Importantly, Fig. 7(b) shows that the steady state eccentricity of the compound drop is hardly influenced by the variation of Ca.

Figure 8 presents the pressure field in the region around the compound drop obtained at $t^* = 8.0$ for Ca = 0.3 and 0.6. It can be clearly observed from Fig. 8 that the pressure inside the inner core drop is higher for Ca = 0.3 in comparison to 0.6. The reduction of pressure inside the inner core with increasing Ca can be anticipated upon consideration of the discontinuity in normal stress at the interface as described by the Young-Laplace equation. The dominating effect of surface tension is strong when the capillary number is small and the pressure difference acting across the interface is proportional to $O(\sigma/R_2)$. The major influence of increasing Ca is to raise the level of pressure inside the drop in comparison to the pressure exterior to the drop.

C. Effect of viscosity ratio

In this section, we explore the impact of the relative viscosity contrast between the shell and ambient fluid on the deformation and steady shape of the compound droplet.
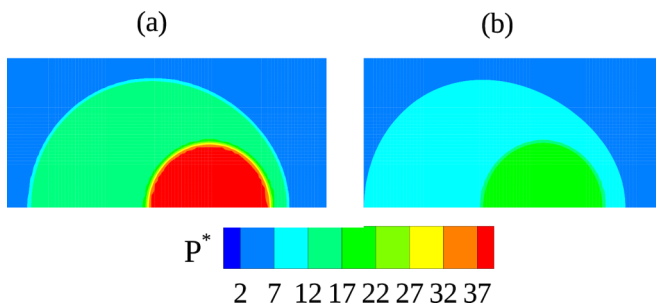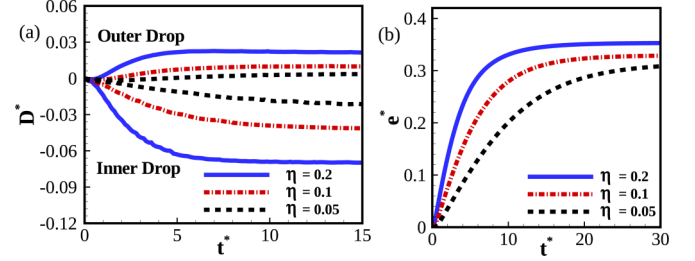
Figures 9(a) and 9(b) show the evolution of D^* and e^*, respectively, for varying η. A decrease in the viscosity ratio leads to significant decrease in the drop deformation as well as eccentricity. This implies that a compound drop traversing in a more viscous ambience tends to deform more significantly as demonstrated in Fig. 9. Furthermore, the magnitude of η controls the temporal rate of evolution of droplet eccentricity. A compound drop with higher η evolves into an eccentric configuration faster than the one with lower η.

To explain the dependence of D^* and e^* on the relative viscosity contrast between the fluids, we analyze the temporal evolution of the average velocities of the inner and outer drops for $\eta = 0.05$ and 0.2 as shown in Fig. 10. It can be clearly discerned that the velocity of the drops for both values of η remains less than the tube centerline velocity in a Poiseuille flow. In the frame of reference of the outer drop, the tube walls move opposite to the drop motion, dragging the fluid at the interface of the drop. The outer drop thus experiences shear from the faster moving continuous fluid as well as shear imposed by the walls of the tube. As the ambience becomes more viscous, the drag force on the interface increases thereby increasing the deformation of the outer drop at higher η. It can also be noted from the inset to Fig. 10 that the inner drop moves faster than the outer drop during the initial moments of migration inside the capillary due to its smaller volume and proximity to the centerline. This relative velocity difference between the inner and outer drop increases at higher
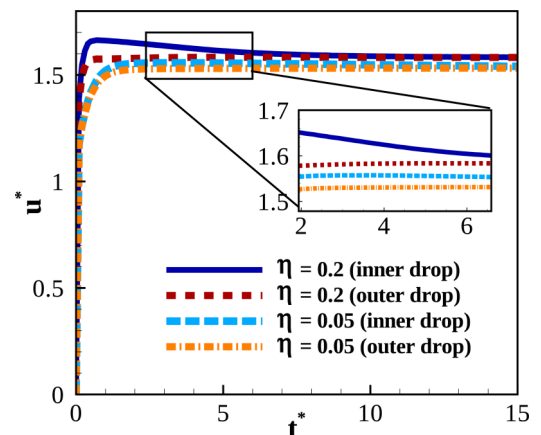

FIG. 8. Contour of pressure (zoomed in the region of the compound drop) at time $t^* = 8.0$ under condition of (a) Ca = 0.3 and (b) Ca = 0.6. The viscosity ratio η is kept fixed at 0.1.

FIG. 10. Temporal evolution of inner and outer drop velocities under varying η. The capillary number is kept fixed at 0.5.

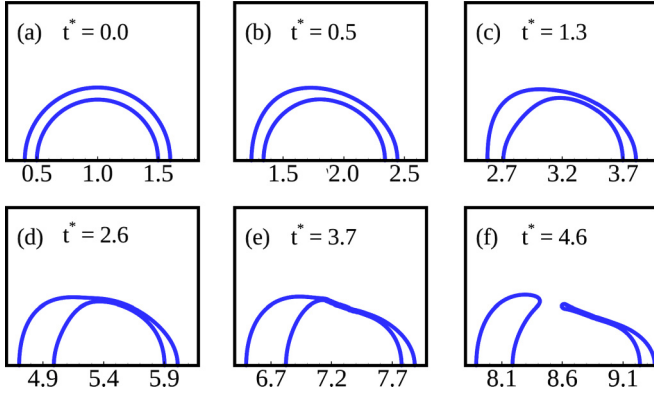FIG. 11. Snapshots showing the temporal evolution of a compound droplet leading to breakup.
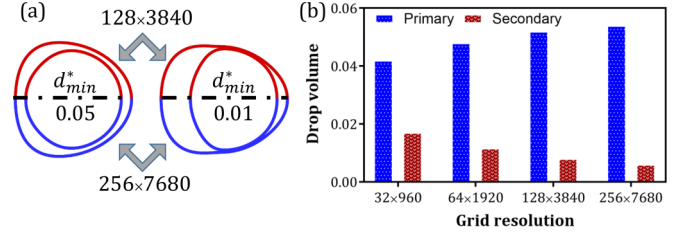

FIG. 12. Grid resolution test for drop breakup. (a) Comparison of drop profile using grid sizes of 128×3840 (upper half) and 256×7680 (lower half). The profiles are plotted for two values of d^*_{min}, 0.05 and 0.01, as the drop proceeds toward breakup. (b) The variation of the volume of primary and secondary drops formed after breakup with different grid resolutions. The capillary number is kept fixed at 0.5.

η and serves as the root cause for the significantly greater deformation of the inner drop due to the large amount of shear acting at the inner interface. The compound droplet undergoes larger deformation if the viscosity of the inner droplet is more or the outer droplet is less viscous.

D. Breakup of compound droplets

The deformation of the inner and outer interfaces of the compound drop depends on the delicate balance between hydrodynamic stresses and interfacial tension. However, this balance may fail under certain conditions leading to breakup of the droplet. We investigate the rupture of the compound droplet during the course of its deformation inside the tube. Figure 11 (and Supplemental Material Video 2 [73]) presents a qualitative picture of the evolution of a compound droplet leading to its eventual breakup. Owing to the opposing nature of deformation of the inner and outer interfaces, the shell thickness becomes nonuniform spatially with increasing eccentricity of the droplet configuration during its temporal evolution. A rapidly thinning region can be clearly observed wherein both the interfaces close in on each other. Eventually, the gap between the two interfaces becomes negligible and the outer shell ruptures to release the inner fluid.

The drop breakup phenomenon is sensitive to the resolution of the numerical grid. To check the convergence of our results, additional grid tests are performed and presented in Fig. 12. We measure the minimum distance between the inner and outer interfaces d^*_{min} (defined in Fig. 5) as the drop proceeds toward breakup and plot the drop profile for $d^*_{min} = 0.05$ and 0.01 for two levels of refinement. The upper and lower half of the drop profile in Fig. 12(a) corresponds to grid-meshes 128×3840 and 256×7680, respectively. It can be clearly observed that the drop profiles are almost identical for the grid sizes 128×3840 and 256×7680, thereby showing convergence of our results. The volume of the primary and secondary drop formed after breakup is computed using different grids and presented in Fig. 12(b). The difference in primary drop volume between grids 32×960 and 64×1920 is $\sim 15\%$, whereas the difference between grid-meshes 128×3840 and 256×7680 is less than 4%. Based on this, the grid-mesh of 128×3840 is used for computing the dynamics of compound drop breakup. The smallest dimensionless cell size for the chosen grid is 0.0078.

Here, we note that the final rupture of the thin liquid sheet will be essentially numerical as the physics that governs the final breakup is molecular and requires multiscale modeling, which hopefully will be possible in the near future. The error introduced due to numerical clipping of the interface is of the order of the smallest grid cell. The present computations shed light on the mechanism of compound droplet breakup and its dependence on relevant parameters.

To gain deeper understanding about the breakup process, we vary the thickness of the shell and examine its effect on the breakup phenomenon. The evolution of d^*_{min} with t^* is presented in Fig. 13(a) for compound droplets with different shell thickness ratio k. Note that a higher value of k denotes a compound drop with smaller shell thickness ($k = R_2/R_1$). A compound drop with higher value of k ruptures in a shorter time due to the smaller distance separating the inner and outer interfaces.

To quantify the thinning rate of the shell, we analyze the relation between the minimum distance between the interfaces d^*_{min} and the time leading to rupture of the shell for $k = 0.73$ and 0.83. The temporal decrease of d^*_{min} with time t^* can be characterized by a power law expression [74] $d^*_{min} \sim \tau^\alpha$, where τ is the time leading to rupture ($\tau = t^*_{rupture} - t^*$) and α is the exponent of power law.
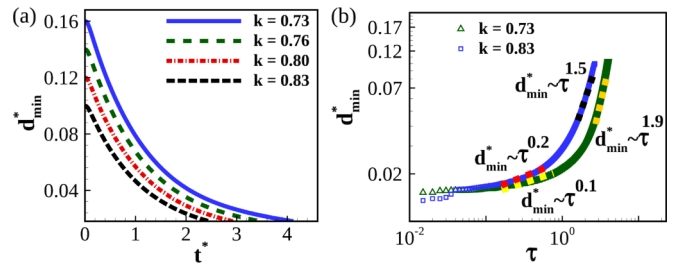

FIG. 13. (a) The temporal evolution of minimum distance between the inner and outer interfaces d^*_{min} for different drops with $k = 0.73, 0.76, 0.80$, and 0.83. (b) Relation between d^*_{min} and time before rupture τ near the breakup of the droplet for $k = 0.73$ and 0.83. The dotted lines in black, orange, red, and yellow represent $d^*_{min} \sim \tau^{1.5}, \tau^{1.9}, \tau^{0.2}$, and $\tau^{0.1}$, respectively. The other operating parameters are Ca = 0.5 and $\eta = 1.0$.
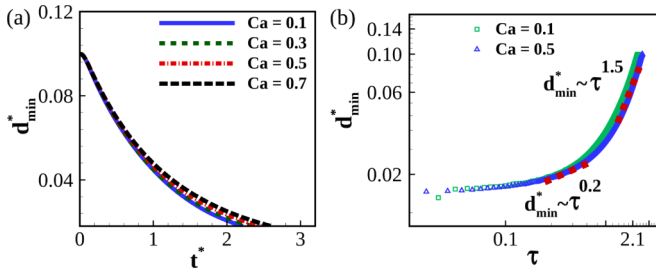
FIG. 14. (a) The temporal evolution of minimum distance between the inner and outer interfaces d^*_{min} for Ca = 0.1, 0.3, 0.5, and 0.7. (b) Relation between d^*_{min} and time before rupture τ near the breakup of the droplet for Ca = 0.1 and 0.5. The dotted lines represents $d^*_{min} \sim \tau^{1.5}$ and $d^*_{min} \sim \tau^{0.2}$. The other operating parameters are $\eta = 1.0$ and $k = 0.83$.

Figure 13(b) depicts the thinning behavior of a compound droplet with $k = 0.73$ and 0.83. During the initial stage of droplet motion, the thinning proceeds at a rapid rate with $\alpha = 1.9$ and 1.5 for $k = 0.73$ and 0.83, respectively. This can be attributed to the high velocity of the inner droplet during the initial moments of the flow which leads to a significant increase of the drop eccentricity. As the inner and outer interfaces approach each other, a thin film is formed near the "nose" of the drop with spatially nonuniform thickness. The flow in this annular thin region is highly squeezed leading to strong viscous stresses. This also explains the higher magnitude of α witnessed for a thicker shell ($k = 0.73$) during the initial duration of thinning in comparison to a thinner shell ($k = 0.80$). Beyond a critical minimum thickness of the film, the thinning rate diminishes with α taking a value of 0.1 and 0.2 for $k = 0.73$ and 0.83, respectively, thereby transitioning into a slowly thinning regime. The influence of Ca on the thinning rate is presented in Fig. 14. It can be observed that the thinning rate is insensitive to the variation of Ca. This can be elucidated by considering the evolution of eccentricity e^* for different Ca as shown in Fig. 7(b). The temporal evolution of e^* is unaffected by the change of Ca, which in turn makes the thinning rate insensitive to Ca. As the magnitude of d^*_{min} decreases, the typical distance separating the interfaces becomes very small compared to the compound drop radius. The pressure inside this small gap is very large, which significantly diminishes the thinning speed as reflected by the rate limiting stage. Eventually, both the interfaces make contact and the film ruptures. The rupture of the thin film can lead to entire draining of the inner core fluid into the surrounding ambient fluid or result in the formation of a smaller compound droplet along with a separate drop of the shell fluid. It may be noted here that herein we attempted only to capture the pinch-off dynamics, because the actual breaking of a compound droplet and the post breakup dynamics require the use of full three dimensional simulations, which falls beyond the scope of the current study.

V. SUMMARY

Numerical simulations have been performed to investigate the hydrodynamic behavior of compound droplets traversing inside a capillary tube under axisymmetric conditions. The study focuses on the temporal evolution of a compound droplet and analyzes its deformation history and interfacial morphologies. The study uncovers an unsteady evolution of a compound droplet under the action of an imposed flow in which the outer droplet progressively deforms along the flow direction attaining a distorted prolate shape. The inner drop, however, gradually deforms perpendicular to the flow direction in the unsteady regime and reaches a distorted oblate shape at steady state. The inner drop moves away from the initial concentric position thereby increasing the drop eccentricity and finally saturates to a constant value with time. The deformation of both the inner and outer interfaces depends on the magnitude of Ca with the inner drop undergoing significantly larger deformation at higher values of Ca. In addition, the viscosity ratio plays a critical role in deciding the magnitude of interfacial deformations and drop eccentricity. The inner drop is found to migrate faster than the outer drop during the initial stage of motion inside the capillary and the relative velocity difference between the drops increases at higher η. The spatiotemporal evolution of the inner drop towards the front of the compound drop and the deformations of the inner and outer interfaces normal to each other forms a thin film near the nose of the moving compound droplet, which eventually causes the breakup of the outer shell of the compound droplet. The thickness of the shell is found to have substantial influence on the stability of the drop thereby determining the time before the outer shell pinches off. However, the rate of thinning is found to be independent of the initial thickness of the shell. Importantly, the rate of thinning of the outer shell thickness follows a power law criterion with one initial stage of swiftly thinning regime to a slowly thinning regime before the pinch-off. The findings from our study may help in predicting the temporal rate of deformation of compound drops traversing inside a capillary. The estimation of rupture time can also be attempted by applying the power-law criterion proposed for compound droplet breakup.

The observations from the present study may stimulate further investigations on the hydrodynamics of compound droplets migrating inside capillary tubes with non-Newtonian rheology. Furthermore, the breakup of compound drops may be explored using full three dimensional simulations along with refined grids which might contribute toward further enhancement of the existing knowledge on compound droplets.

ACKNOWLEDGMENTS

[1] B. Damit, Aerosol Sci. Technol. **51**, 488 (2017).

[2] W. D. Wu, K. C. Patel, S. Rogers, and X. D. Chen, Drying Technol. **25**, 1907 (2007).

[3] E. Brouzes, M. Medkova, N. Savenelli, D. Marran, M. Twardowski, J. B. Hutchison, J. M. Rothberg, D. R. Link, N. Perrimon, and M. L. Samuels, Proc. Natl. Acad. Sci. USA **106**, 14195 (2009).

[4] J. Clausell-Tormos, D. Lieber, J.-C. Baret, A. El-Harrak, O. J. Miller, L. Frenz, J. Blouwolff, K. J. Humphry, S. Köster, H. Duan *et al.*, Chem. Biol. **15**, 427 (2008).

[5] A. G. Sciancalepore, A. Polini, E. Mele, S. Girardo, R. Cingolani, and D. Pisignano, Biosens. Bioelectron. **26**, 2711 (2011).

[6] R. Prakash, K. Pabbaraju, S. Wong, A. Wong, R. Tellier, and K. V. Kaler, Micromachines **6**, 63 (2014).

[7] K. F. Jensen, Chem. Eng. Sci. **56**, 293 (2001).

[8] X. Niu, M. Zhang, J. Wu, W. Wen, and P. Sheng, Soft Matter **5**, 576 (2009).

[9] J. Xu, S. Li, J. Tan, Y. Wang, and G. Luo, Langmuir **22**, 7943 (2006).

[10] A. Utada, E. Lorenceau, D. Link, P. Kaplan, H. Stone, and D. Weitz, Science **308**, 537 (2005).

[11] R. K. Shah, H. C. Shum, A. C. Rowat, D. Lee, J. J. Agresti, A. S. Utada, L.-Y. Chu, J.-W. Kim, A. Fernandez-Nieves, C. J. Martinez *et al.*, Materials Today **11**, 18 (2008).

[12] L.-Y. Chu, A. S. Utada, R. K. Shah, J.-W. Kim, and D. A. Weitz, Angew. Chem. Int. Ed. Engl. **46**, 8970 (2007).

[13] A. Frohn and N. Roth, *Dynamics of Droplets* (Springer Science & Business Media, Berlin, 2000).

[14] C. Zhou, P. Yue, and J. J. Feng, Phys. Fluids **18**, 092105 (2006).

[15] A. R. Abate, J. Thiele, and D. A. Weitz, Lab Chip **11**, 253 (2011).

[16] M. Azarmanesh, M. Farhadi, and P. Azizian, Int. J. Numer. Methods Heat Fluid Flow **25**, 1705 (2015).

[17] A. Abate and D. Weitz, Small **5**, 2030 (2009).

[18] J. M. Park and P. D. Anderson, Lab Chip **12**, 2672 (2012).

[19] Y. Zhang, H. F. Chan, and K. W. Leong, Adv. Drug Delivery Rev. **65**, 104 (2013).

[20] D. Lee and D. A. Weitz, Adv. Mater. **20**, 3498 (2008).

[21] H. C. Shum, Y.-j. Zhao, S.-H. Kim, and D. A. Weitz, Angew. Chem. **123**, 1686 (2011).

[22] A. R. Abate, J. Thiele, M. Weinhart, and D. A. Weitz, Lab Chip **10**, 1774 (2010).

[23] S.-H. Kim, H. C. Shum, J. W. Kim, J.-C. Cho, and D. A. Weitz, J. Am. Chem. Soc. **133**, 15165 (2011).

[24] V. Sinha and A. Kumar, Indian J. Pharm. Sci. **64**, 191 (2002).

[25] G. Hetsroni, S. Haber, and E. Wacholder, J. Fluid Mech. **41**, 689 (1970).

[26] H. Brenner, Ind. Eng. Chem. Fundam. **10**, 537 (1971).

[27] W. A. Hyman and R. Skalak, Appl. Sci. Res. **26**, 27 (1972).

[28] M. J. Martinez and K. S. Udell, J. Fluid Mech. **210**, 565 (1990).

[29] T. M. Tsai and M. J. Miksis, J. Fluid Mech. **274**, 197 (1994).

[30] H. Zhou and C. Pozrikidis, Phys. Fluids **6**, 80 (1994).

[31] S. Mortazavi and G. Tryggvason, J. Fluid Mech. **411**, 325 (2000).

[32] A. J. Griggs, A. Z. Zinchenko, and R. H. Davis, Int. J. Multiphase Flow **33**, 182 (2007).

[33] E. Lac and J. Sherwood, J. Fluid Mech. **640**, 27 (2009).

[34] B. Nath, G. Biswas, A. Dalal, and K. C. Sahu, Phys. Rev. E **95**, 033110 (2017).

[35] A. Karnis, H. L. Goldsmith, and S. G. Mason, Nature **200**, 159 (1963).

[36] B. P. Ho and L. G. Leal, J. Fluid Mech. **71**, 361 (1975).

[37] W. L. Olbricht, Annu. Rev. Fluid Mech. **28**, 187 (1996).

[38] H. Stone and L. Leal, J. Fluid Mech. **211**, 123 (1990).

[39] J. Wang, J. Liu, J. Han, and J. Guan, Phys. Rev. Lett. **110**, 066001 (2013).

[40] K. A. Smith, J. M. Ottino, and M. Olvera de la Cruz, Phys. Rev. Lett. **93**, 204501 (2004).

[41] Y. Chen, X. Liu, C. Zhang, and Y. Zhao, Lab Chip **15**, 1255 (2015).

[42] H. Hua, J. Shin, and J. Kim, Int. J. Heat Fluid Flow **50**, 63 (2014).

[43] Y. Chen, X. Liu, and Y. Zhao, Appl. Phys. Lett. **106**, 141601 (2015).

[44] S. Tasoglu, G. Kaynak, A. J. Szeri, U. Demirci, and M. Muradoglu, Phys. Fluids **22**, 082103 (2010).

[45] P. Gao and J. J. Feng, J. Fluid Mech. **682**, 415 (2011).

[46] S. K. Veerapaneni, Y.-N. Young, P. M. Vlahovska, and J. Błatwdziewicz, Phys. Rev. Lett. **106**, 158103 (2011).

[47] M. Levant and V. Steinberg, Phys. Rev. Lett. **112**, 138106 (2014).

[48] Z. Y. Luo, L. He, and B. F. Bai, J. Fluid Mech. **775**, 77 (2015).

[49] Z. Y. Luo and B. F. Bai, Phys. Fluids **28**, 101901 (2016).

[50] L. Zhu and F. Gallaire, Phys. Rev. Lett. **119**, 064502 (2017).

[51] O. M. Lavrenteva, L. Rosenfeld, and A. Nir, Phys. Rev. E **84**, 056323 (2011).

[52] S. Mandal, U. Ghosh, and S. Chakraborty, J. Fluid Mech. **803**, 200 (2016).

[53] J. Tao, X. Song, J. Liu, and J. Wang, Chem. Eng. Sci. **97**, 328 (2013).

[54] J. Li, H. Chen, and H. A. Stone, Langmuir **27**, 4324 (2011).

[55] S. Sadhal and H. Oguz, J. Fluid Mech. **160**, 511 (1985).

[56] R. E. Johnson and S. Sadhal, Annu. Rev. Fluid Mech. **17**, 289 (1985).

[57] S. Sadhal *et al.*, J. Fluid Mech. **179**, 105 (1987).

[58] Y. Song, J. Xu, and Y. Yang, Phys. Fluids **22**, 072003 (2010).

[59] N. Oba, H. Sugimura, Y. Umehara, M. Yoshida, T. Kimura, and T. Yamaguchi, Lipids **27**, 701 (1992).

[60] N. Bhatia, S. Pandit, S. Agarwal, and D. Gupta, Int. J. Pharmaceut. Erudition **3**, 22 (2013).

[61] S. Popinet, "Basilisk" retrieved from, http://basilisk.fr.

[62] S. Popinet, J. Comput. Phys. **190**, 572 (2003).

[63] S. Popinet, J. Comput. Phys. **302**, 336 (2015).

[64] C. J. Howland, A. Antkowiak, J. R. Castrejón-Pita, S. D. Howison, J. M. Oliver, R. W. Style, and A. A. Castrejón-Pita, Phys. Rev. Lett. **117**, 184502 (2016).

[65] P. K. Farsoiya, Y. Mayya, and R. Dasgupta, J. Fluid Mech. **826**, 797 (2017).

[66] J. B. Bell, P. Colella, and H. M. Glaz, J. Comput. Phys. **85**, 257 (1989).

[67] C. W. Hirt and B. D. Nichols, J. Comput. Phys. **39**, 201 (1981).

[68] J. Brackbill, D. B. Kothe, and C. Zemach, J. Comput. Phys. **100**, 335 (1992).

[69] D. B. Khismatullin and G. A. Truskey, Biophys. J. **102**, 1757 (2012).

[70] A. Evangelio, F. Campo-Cortés, and J. Gordillo, J. Fluid Mech. **804**, 550 (2016).

[71] W. Olbricht and D. Kung, Phys. Fluids A **4**, 1347 (1992).

[72] A. Nadim and H. A. Stone, Stud. Appl. Math. **85**, 53 (1991).

[73] See Supplemental Material at http://link.aps.org/supplemental/10.1103/PhysRevE.97.043112 for additional information.

[74] M. P. Borthakur, G. Biswas, and D. Bandyopadhyay, Phys. Rev. E **96**, 013115 (2017).